ACS APPLIED MATERIALS & INTERFACES

Research Article

www.acsami.org

Self-Templated Growth of Vertically Aligned 2H-1T MoS_2 for Efficient Electrocatalytic Hydrogen Evolution

Jing Yang,[†] Kai Wang,[†] Jixin Zhu,[‡] Chao Zhang,[*,†] and Tianxi Liu[*,†]

[†] State Key Laboratory for Modification of Chemical Fibers and Polymer Materials, College of Materials Science and Engineering, Donghua University, Shanghai 2016620, P. R. China

[‡] Key Laboratory of Flexible Electronics (KLOFE) & Institute of Advanced Materials (IAM), Jiangsu National Synergetic Innovation Center for Advanced Materials (SICAM), Nanjing Tech University (Nanjing Tech), 30 South Puzu Road, Nanjing 211816, P. R. China

Ⓢ *Supporting Information*

ABSTRACT: Semiconductor heterostructures of two-dimensional (2D) transition metal disulfide (TMD) have opened up approaches toward the integration of each function and implementations in novel energy and electronic devices. However, engineering TMD-based homostructures with tailored properties is still challenging. Herein, we demonstrate a solution-processed growth of vertically aligned 1T-MoS_2 using liquid-phase exfoliated 2H-MoS_2 as self-templates. The unique MoS_2-based homostructures not only provide more exposed active sites in the edge and basal plane for the electrocatalytic hydrogen evolution reaction (HER) but also improve the mass transfer due to the introduction of high packing porosity. The resultant all-MoS_2 electrocatalysts with an integration of polymorphous MoS_2 nanostructures exhibit a superior HER activity with a low potential of 203 mV at 10 mA cm^{-2}, a small Tafel slope of 60 mV dec^{-1}, and a remarkable cyclic stability. This work thus provides a simple and efficient route for the creation of unprecedented MoS_2-based homostructured materials with exciting properties, especially as an inexpensive alternative to platinum catalysts in electrochemical hydrogen evolution production.

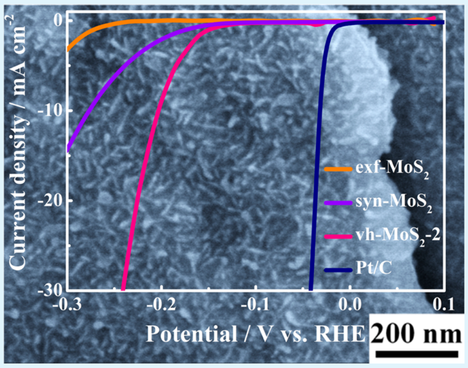

KEYWORDS: *molybdenum disulfide, liquid-phase exfoliation, self-templated growth, vertical alignment, hydrogen evolution reaction*

1. INTRODUCTION

In recent years, hydrogen has been regarded as the most promising future energy source because of its high efficiency, environmental friendliness, and renewability.[1−4] The selection and development for efficient catalysts of hydrogen evolution electrode in direct electrolytic water splitting is the most important factor for producing hydrogen.[5−7] Platinum-group precious metals exhibit good electrocatalytic activity toward the hydrogen evolution reaction (HER), but their expensive costs and resource scarcities have greatly limited their practical applications.[6,8−10] Therefore, it is urgent to develop an efficient, inexpensive, and earth-abundant electrocatalyst with a low overpotential and optimized catalytic process.[11−14]

Monolayer molybdenum disulfide (MoS_2) is a promising two-dimensional direct band gap semiconductor with various potential applications,[15−17] such as in lithium ion batteries,[18−21] supercapacitors,[22−24] and catalysts.[25−27] Due to similar Gibbs free energy for hydrogen adsorption to platinum, MoS_2 has been especially served as an efficient catalyst for HER.[28−32] An increase of the number of exposed edge sites by tuning the microstructure, the dimension, and the exposed grain surfaces plays important roles in tuning the catalytic activity toward HER.[33−38] Unfortunately, due to the severe aggregation of individual MoS_2 nanosheets, it is difficult to approach a limit of MoS_2 catalyst with as many exposed active sites as possible. Besides, the poor conductivity of the semiconductive 2H-phase MoS_2 of the most commonly naturally occurring polytype MoS_2 greatly limits the performance of the catalysts.[37,39] Therefore, it is of great importance to adopt strategies to increase the conductivity of catalysts and the density of catalytic active sites by a rational design of the resultant MoS_2-based electrocatalysts.[40−45] Very recently, the construction of the vertical heterostructure of 2D MoS_2 has drawn much attention because such an anisotropic stacking form gives rise to orientation-dependent functionalities of the 2D materials.[31,39,46,47] Different from most researches on 2D MoS_2 materials with other 2D layered materials for constructing heterostructures using relatively easier synthesis methods, engineering MoS_2-based homostructures with tailored properties is still challenging and has been rarely reported.

Herein, a simple and efficient strategy for growth of fewer-layer 1T-phase solvothermally synthesized MoS_2 (abbreviated as syn-MoS_2) onto 2H-phase liquid-exfoliated MoS_2 (abbreviated as exf-MoS_2) has been proposed. This method by

Received: September 6, 2016
Accepted: November 1, 2016
Published: November 1, 2016

DOI: 10.1021/acsami.6b11298
ACS Appl. Mater. Interfaces 2016, 8, 31702−31708

combining all 2D MoS_2 into homostructures with polymorphous crystal phases offers at least three advantages over traditional methods for the synthesis of hierarchically nanostructured MoS_2 reported in the literature: (1) Growing syn-MoS_2 on exf-MoS_2 develops a homostructure with hierarchical nanostructures and exciting properties. (2) The vertically aligned syn-MoS_2 on exf-MoS_2 provides an edge-to-edge structure with more exposed active sites. (3) The immobilized metallic 1T-phase syn-MoS_2 improves the conductivity of the homostructures to facilitate the electron transport and introduce efficient mass transfer channels of electrolytes.

2. EXPERIMENTAL SECTION

2.1. Preparation of Monolayer and Few-Layer exf-MoS_2. The monolayer and few-layer exf-MoS_2 nanosheets were prepared by a liquid-phase sonication exfoliation of bulk molybdenites (1.0 g) in *N*,*N*-dimethylformamide (DMF) (100 mL). After a bath sonication for 6 h, the suspension was centrifuged at 1500 rpm for 15 min to remove impurities, and the supernatant was left aside for the subsequent use. The concentration of exf-MoS_2 in the supernatant was measured as ~0.80 mg mL^{-1} by drying a designed volume of the supernatant on a preweighted glass Petri dish in a 110 °C oven and then weighting the residuals.

2.2. Preparation of Vertically Aligned Homostructured MoS_2 (vh-MoS_2). The solvothermal growth of few-layer syn-MoS_2 on exf-MoS_2 for the preparation of vh-MoS_2 was presented as follows. The mass ratios of exf-MoS_2 to syn-MoS_2 within the vh-MoS_2 products were controlled by changing the initial concentrations of exf-MoS_2 in DMF. Typically, a designed volume of the supernatant of exf-MoS_2 was diluted into 80 mL with DMF, followed by the addition of 80 mg of $(NH_4)_2MoS_4$ and 0.8 mL of 50 wt % hydrazine hydrate under stirring. Then, the mixture was transferred into a 100 mL Teflon-lined stainless steel autoclave and heated in an oven at 200 °C for 10 h. The products were collected by filtration, washed with excess DMF and ethanol, and dried at 60 °C in a vacuum oven overnight. The initial volumes of the supernatant of exf-MoS_2 were selected as 40, 20, and 10 mL, respectively, and the resultant products were denoted as vh-MoS_2-1, vh-MoS_2-2, and vh-MoS_2-3, respectively. Neat syn-MoS_2 was prepared for comparison under the same solvothermal condition in the absence of exf-MoS_2.

3. RESULTS AND DISCUSSION

The synthesis of vertically aligned syn-MoS_2 on exf-MoS_2 for the construction of vh-MoS_2 mainly consists of two steps, as shown in Figure 1. As exhibited in Figure 1a, monolayer and few-layer exf-MoS_2 nanosheets are obtained by a sonication-assisted exfoliation of bulk MoS_2 in an appropriate solvent such as DMF.[48−50] A sediment experiment of exf-MoS_2 in DMF is preferentially investigated by observing the exf-MoS_2 dispersion after left standing for 2 weeks. The exf-MoS_2 in DMF keeps a well-dispersed condition without any precipitations (Figure S1). The exf-MoS_2 (Figure S2) exhibits a nanoflake structure, indicating the successful exfoliations from bulk MoS_2 via liquid-phase sonication. A solvothermal synthesis of MoS_2 in the absence of exf-MoS_2 always produces 2H-phase syn-MoS_2 (Figure 1b). The as-grown syn-MoS_2 nanosheets (Figure S3) self-assemble into a nanoflower structure. As shown in Figure 1c, exf-MoS_2 and ammonium thiomolybdate are utilized as template and precursor, respectively, for the solution-processed growth of vh-MoS_2. Eventually, few-layer 1T-phase syn-MoS_2 are successfully vertically aligned on the exf-MoS_2 template, providing high surface area with abundant active sites in both edges and basal planes. The mass ratios of exf-MoS_2 and syn-MoS_2 within the vh-MoS_2 are tuned, and the resultant products are denoted as vh-MoS_2-1, vh-MoS_2-2, and vh-MoS_2-3, respectively. Figures S4c and S4d show the morphology of the vh-MoS_2-2 at different magnifications, which exhibits a hierarchical structure with ultrathin, interconnected, and wrinkled syn-MoS_2 uniformly coated on large-lateral exf-MoS_2. No obvious MoS_2 agglomerates could be observed on the whole, indicating that exf-MoS_2 nanosheets serve as ideal templates for the efficient immobilization of in situ grown syn-MoS_2. The morphologies of the vh-MoS_2 with different contents of exf-MoS_2 are systematically investigated. For the vh-MoS_2-1 sample (Figures S4a and S4b) with sufficient exf-MoS_2 templates, only sparse syn-MoS_2 nanosheets are found on exf-MoS_2 nanosheets. Conversely, as evidenced in Figures S4e and S4f, redundant syn-MoS_2 nanosheets among the vh-MoS_2-3 sample tend to stack together forming a nanoflower structure. The nitrogen adsorption/desorption isotherms of exf-MoS_2, syn-MoS_2, and vh-MoS_2-2 are measured and shown in Figure S5a. The data of the BET surface areas and their pore size distributions of these samples are summarized in Table 1. The vh-MoS_2-2 exhibits an obviously enlarged specific surface area of 62.2 m^2 g^{-1}, which is obviously larger than that of exf-MoS_2 (43.5 m^2 g^{-1}) and syn-MoS_2 (31.5 m^2 g^{-1}), indicating that the exf-MoS_2 can be considered as an effective template for the sequent decoration of the all-MoS_2 hierarchical nanostructures with increased surface areas. As shown in Figure S5b and Table 1, the enlarged pore volume with both micropores and mesopores may also make contributions to the enhanced electrocatalytic performances.

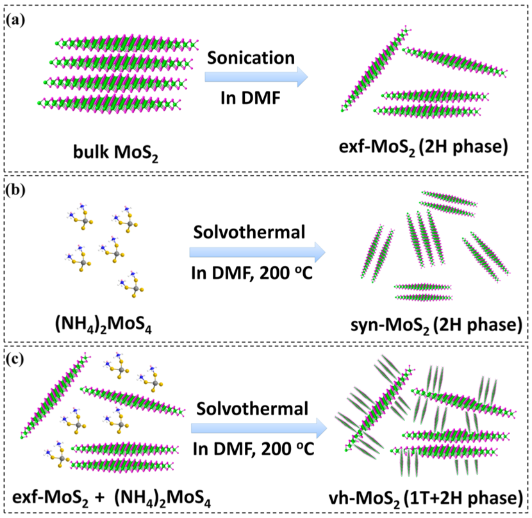

Figure 1. Illustration of solution-processed synthesis of vh-MoS_2. (a) Schematic liquid-phase exfoliation of bulk MoS_2 into exf-MoS_2 nanosheets. (b) Schematic solvothermal synthesis of syn-MoS_2 nanosheets. (c) Schematic solvothermal synthesis of vh-MoS_2 in the presence of exf-MoS_2 nanosheets.

Table 1. BET Surface Areas and Pore Size Distributions of exf-MoS_2, syn-MoS_2, and vh-MoS_2-2

samples	S_{BET} [m^2 g^{-1}]	total pore volume [mL g^{-1}]	micropore volume [mL g^{-1}]	mesopore volume [mL g^{-1}]
exf-MoS_2	43.5	0.12	0.002	0.12
syn-MoS_2	31.5	0.15	0	0.15
vh-MoS_2-2	62.2	0.20	0.01	0.19

The morphologies of MoS_2 homostructures were further investigated by TEM observations. Figure 2a indicates that exf-

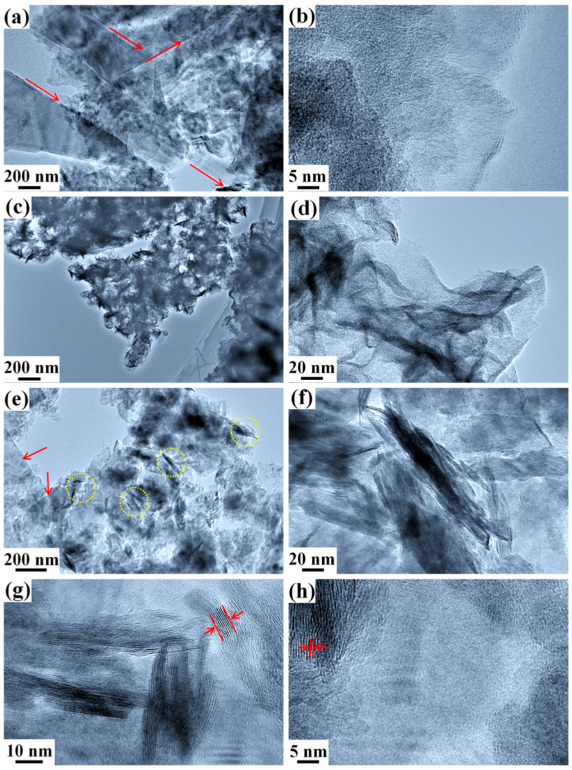

Figure 2. TEM images of (a, b) exf-MoS_2, (c, d) syn-MoS_2, and (e, f) vh-MoS_2-2 at low and high magnifications, respectively, and (g, h) HRTEM images of vh-MoS_2-2.

MoS_2 nanosheets with a large lateral size of several micrometers are exfoliated well, and even monolayer edges could be observed (red arrows in Figure 2a and enlarged in Figure 2b). Neat syn-MoS_2 displays a flower-like morphology composed of massive wrinkled MoS_2 nanosheets (Figure 2c and 2d). From Figure 2e and 2f, it can be clearly seen that among the vh-MoS_2-2 sample the perpendicularly oriented MoS_2 nanosheets (marked by yellow circle) are vertically aligned on exf-MoS_2 (marked by red arrows) without agglomeration and restacking, which are consistent with SEM results of vh-MoS_2-2 (Figure S4c and S4d). Besides, the HRTEM images of the vh-MoS_2-2 sample in Figure 2g and 2h clearly exhibit a large quantity of exposed edge sites of the (002) plane. The perpendicularly oriented MoS_2 nanosheets are composed of fewer layers (5−15 layers) with the interlayer spacing of 0.65 nm (marked by red arrows).

The growth mechanism of syn-MoS_2 on exf-MoS_2 is intensively investigated, and the self-standing exf-MoS_2 film is fabricated and used as macroscopic templates to grow syn-MoS_2. The exf-MoS_2 film with preferential plane orientation is fabricated by directly casting the exf-MoS_2 suspension on copper foil via a drying-induced self-assembly process. Compared with monolayer and few-layer exf-MoS_2 nanosheets, exf-MoS_2 film provides more flat and large surface for the direct immobilization of syn-MoS_2, and therefore it is more convenient to observe the morphology of immobilized syn-MoS_2 at a relatively large scale. As shown in Figure 3, after in situ growth of syn-MoS_2, close inspections from SEM images show that the surface of exf-MoS_2 film is uniformly covered with syn-MoS_2 arrays with their *ab*-faces perpendicular and parallel to the exf-MoS_2. An evolution selection process is further employed here to explain the vertical growth mechanism of syn-MoS_2 arrays on exf-MoS_2. The nucleation density of syn-MoS_2 on the basal planes of exf-MoS_2 significantly increases, and thus *ab*-planes of syn-MoS_2 perpendicular to the template become dominant on the exf-MoS_2 surface.

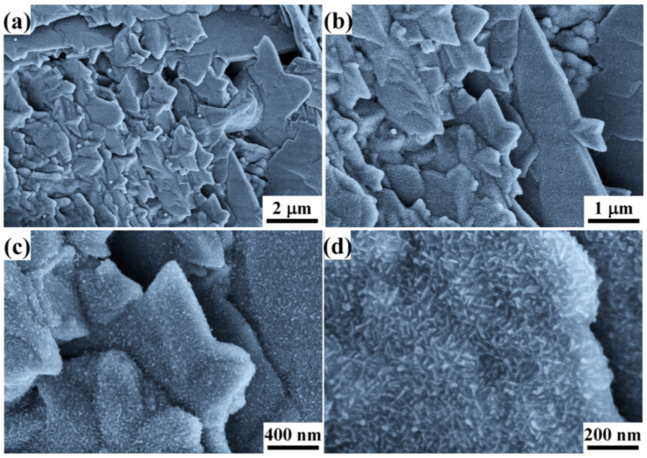

Figure 3. SEM images of vertical aligned MoS_2 nanosheets grown on the exf-MoS_2 film with a (a) 15 000, (b) 30 000, (c) 75 000, and (d) 150 000 magnification. The SEM images clearly proved that syn-MoS_2 in the form of vertical aligned nanostructures was successfully grown on the exf-MoS_2 templates.

The crystalline phase identity was further confirmed using XRD patterns and Raman spectroscopy. Figure 4a exhibits the XRD patterns of exf-MoS_2, syn-MoS_2, and vh-MoS_2, respectively. A 2H-phase of MoS_2 is clearly indicated in the exf-MoS_2 sample evidenced by diffraction peaks at 2θ = 14.4, 32.7, 39.5, 49.8, 58.3, and 60.2°, which correspond to the (002), (100), (103), (105), (110), and (008) planes of 2H-MoS_2 crystal phase (JCPDS Card No. 37-1492). The XRD pattern of neat syn-MoS_2 displays weak diffraction peaks at 2θ = 32.7 and 56.8° assigned to the (100) and (110) planes, respectively, which reveal a hexagonal lattice structure with a spacing of 0.27 nm and unvaried atomic arrangement along the basal planes.[51] The (002) plane attributed to the interlayer

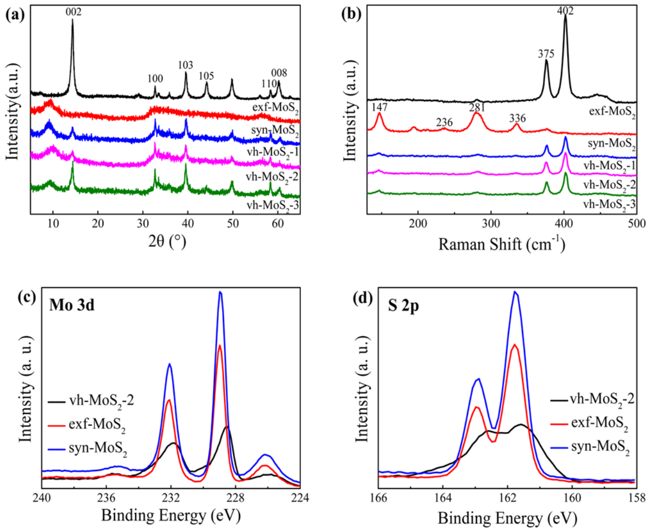

Figure 4. (a) XRD patterns and (b) Raman spectra of exf-MoS_2, syn-MoS_2, and vh-MoS_2 samples. XPS spectra of (c) Mo 3d and (d) S 2p of exf-MoS_2, syn-MoS_2, and vh-MoS_2-2.

spacing is almost negligible, suggesting a low crystallinity of MoS_2. In addition, a new peak at $2\theta = 9.3°$ with an interlayer spacing of 0.95 nm is clearly observed, indicating the formation of a new lamellar structure with an increased interplanar spacing compared to that of hexagonal MoS_2 (0.62 nm).[52] Therefore, the crystalline phase of syn-MoS_2 could not be determined here, and it has been reported that the significantly enhanced interlayered spacing might be due to different solvothermal synthesis conditions. For example, Xie's group points out that the reaction temperature below 220 °C could result in an enlarged interlayer spacing.[42] Moreover, the expanded interlayer is likely attributed to the intercalation of oxidized DMF species into two S−Mo−S layers.[53] Therefore, both the relatively low reaction temperature (200 °C) and the intercalated DMF species in our work might lead to the expansion of interlayer spacing of syn-MoS_2. It is also worth noticing that the vh-MoS_2 samples basically retain the combination of the diffraction peaks of both exf-MoS_2 and syn-MoS_2 phases, while the intensity of the (002) diffraction peak ascribed to exf-MoS_2 decreases, indicating that the syn-MoS_2 nanosheets considerably inhibit the restacking of exf-MoS_2 within the MoS_2 homostructures. Figure 4b exhibits the Raman curves taken from exf-MoS_2, syn-MoS_2, and vh-MoS_2 samples. The characteristic peaks of exf-MoS_2 at 375 and 402 cm^{-1} corresponding to in-plane E_{2g}^{1} and out-of-plane A_{1g}, respectively, are in agreement with those of 2H-phase MoS_2. The separation (ca. 27 cm^{-1}) between the E_{2g}^{1} and A_{1g} modes reveals a few-layer feature of MoS_2 according to recent studies.[54,55] Moreover, the additional weak Raman shifts emerging at 147 (J_1), 236 (J_2), 281 (E_{1g}), and 336 (J_3) cm^{-1} indicate that there exists 1T-phase MoS_2 within neat syn-MoS_2 and vh-MoS_2.[24,26,35,56−59] The Raman results indicate that a thermodynamic unstable 1T-phase MoS_2 might exist within the vh-MoS_2 samples due to the presence of exf-MoS_2 templates.

X-ray photoelectron spectroscopy (XPS) measurements, an efficient method to distinguish 2H and 1T polymorphs of MoS_2, were conducted to further investigate the crystalline compositions and valence states of the resulting MoS_2 samples. The typical XPS spectra of Mo 3d (Figure 4c) and S 2p (Figure 4d) prove the formation of MoS_2 by calculating the peak area of Mo 3d and S 2p. From the XPS spectra of exf-MoS_2 and syn-MoS_2, it could be observed that the characteristic peaks at 232.1 and 228.9 eV correspond to the binding energies of Mo $3d_{3/2}$ and Mo $3d_{5/2}$ orbitals of 2H-MoS_2, respectively, confirming the formation of Mo^{4+}. The XPS peaks of vh-MoS_2-2 manifest the coexistence of 1T-phase and 2H-phase MoS_2 in the hybrid as the binding energies of Mo $3d_{3/2}$ and Mo $3d_{5/2}$ orbitals shift to 231.8 and 228.5 eV, which are slightly lower than those of 2H-phase MoS_2.[37] The corresponding peaks for the S $2p_{1/2}$ and S $2p_{3/2}$ orbitals of vh-MoS_2-2 also shift from 162.9 and 161.8 eV to 162.6 and 161.6 eV, respectively, indicating the existence of Mo−S bonding instead of elemental S.[60] The vh-MoS_2-2 sample shows the characteristic peaks of Mo 3d and S 2p combining 2H-phase and 1T-phase MoS_2, indicating that the existence of the exf-MoS_2 template promotes the formation and stability of thermodynamic unstable 1T-phase MoS_2 within the vh-MoS_2 samples.

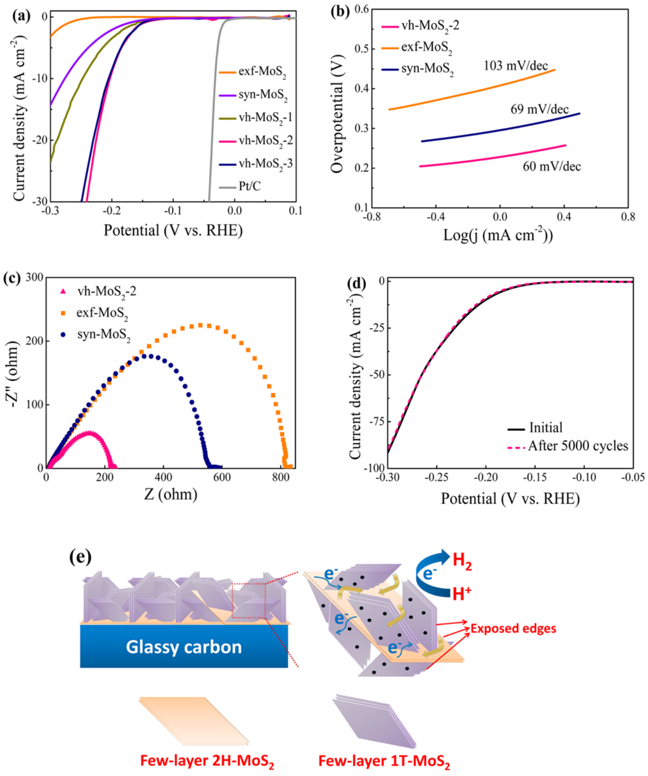

Figure 5. (a) Polarization curves of exf-MoS_2, syn-MoS_2, vh-MoS_2, and Pt/C electrode with a scan rate of 2 mV s^{-1}. (b) The corresponding Tafel plots from the polarization curves with a scan rate of 0.5 mV s^{-1} for exf-MoS_2, syn-MoS_2, and vh-MoS_2-2. (c) Nyquist plots of exf-MoS_2, syn-MoS_2, and vh-MoS_2-2 electrodes for the HER carried out at an overpotential of 0.25 V. (d) Polarization curves of vh-MoS_2-2 electrode initially and after 5000 cycles between −0.05 and −0.30 V at a scan rate of 50 mV s^{-1}. (e) Schematic representation of the vh-MoS_2 electrode with hierarchical nanostructures fastening fast electron and mass transport between the vertically aligned nanodomains.

In order to evaluate the electrochemical catalytic activities of the vh-MoS_2 samples, the polarization curves of vh-MoS_2, exf-MoS_2, syn-MoS_2, and commercial Pt/C samples were measured in a N_2-saturated 0.5 M H_2SO_4 electrolyte. As shown in Figure 5a, the Pt/C catalyst exhibits superior catalytic performance for HER with a near zero onset potential and a small overpotential of 32 mV at 10 mA cm^{-2}. The bulk MoS_2 shows almost no HER activity in the selected voltage range, while the exf-MoS_2 shows a slightly enhanced catalytic activity compared to bulk MoS_2, which is attributed to increased exposed active sites generated by the exfoliation.[33,61] The syn-MoS_2 electrode exhibits an ordinary HER activity with an onset potential of 129 mV and an overpotential of 276 mV at 10 mA cm^{-2}. The vh-MoS_2 samples exhibit much better activity than bare exf-MoS_2 and syn-MoS_2 samples, indicating a fantastic synergistic effect of combining 1T- and 2H-phase MoS_2. The influences of the contents of exf-MoS_2 on the catalytic performances of the resultant vh-MoS_2 are also investigated. As shown in Figure 5b, the vh-MoS_2-1, vh-MoS_2-2, and vh-MoS_2-3 electrodes exhibit low onset overpotentials of 119, 116, and 122 mV, respectively (determined from the Tafel plots, as shown in Figure S6). Moreover, the vh-MoS_2-2 electrode represents more efficient catalytic performance with a low overpotential of 202 mV at 10 mA cm^{-2} compared with those of vh-MoS_2-1 (248 mV) and vh-MoS_2-3 (205 mV). Therefore, the weight contents of exf-MoS_2 within vh-MoS_2 play important roles in determining the final catalytic performances. The vh-MoS_2-2 sample leads to a relatively low overpotential because uniformly immobilized syn-MoS_2 nanosheets on exf-MoS_2 might produce more exposed active sites. The relatively large contents of exf-MoS_2 within vh-MoS_2-1 lead to a weaker performance since excessive exf-MoS_2 templates inherently exhibit a poor HER activity. Likewise, the syn-MoS_2 within vh-MoS_2-3 tending to stack together inherently weakens the HER activity. Tafel slopes could give more information to investigate the dramatic improvement of the catalytic performances with the combination of 1T- and 2H-phase MoS_2. There are three reaction mechanisms for the generation of hydrogen by water splitting. The first step is a discharge step (Volmer reaction) with a Tafel slope of ~120 mV per decade, $H_3O^+ + e^- \rightarrow H_{ads} + H_2O$, where a proton is absorbed on an active site of MoS_2 edges. The following step involves an electrochemical desorption step (Heyrovsky reaction) with a Tafel slope of ~40 mV per decade, $H_{ads} + H_3O^+ + e^- \rightarrow H_2 + H_2O$, or a Tafel recombination step (Tafel reaction) with a Tafel slope of ~30 mV per decade, $H_{ads} + H_{ads} \rightarrow H_2$. As shown in Figure 4b, the Tafel slope obtained for vh-MoS_2-2 is ~60 mV dec^{-1}, while exf-MoS_2 and syn-MoS_2 catalysts possess a larger Tafel slope of 103 and 69 mV dec^{-1}, respectively. With a Tafel slope of ~60 mV dec^{-1}, the HER process of the vh-MoS_2-2 catalyst is ascribed to follow the Volmer−Herovsky reaction mechanism with an electrochemical desorption as the rate-determining step. The lower onset overpotential and smaller Tafel slope of the vh-MoS_2 is attributed to the synergistic effect of 2H- and 1T-phase MoS_2 in vh-MoS_2 samples with more exposed active sites and improved electron transport pathways. The improved electron transport pathways of the vh-MoS_2 sample are confirmed using an AC impedance measurement. The Nyquist plots in Figure 5c reveal that vh-MoS_2-2 exhibits a dramatically decreased charge transfer resistance (R_{ct}) of 222 Ω in comparison with those of neat syn-MoS_2 (557 Ω) and exf-MoS_2 (816 Ω), indicating faster electrode kinetics due to the presence of metallic 1T-MoS_2 in vh-MoS_2-2.[62] We also study the effects of introducing conducting additives on the final performance of the homostructured MoS_2-based catalysts. It should be noted that with the addition of conductive additives such as commercial carbon black the HER electrocatalytic performance is distinctly enhanced. As shown in Figure S7, the vh-MoS_2-2 electrode with carbon black exhibits better catalytic performance with a low overpotential of 188 mV at 10 mA cm^{-2} compared with that of the neat vh-MoS_2-2 electrode (202 mV at 10 mA cm^{-2}). We also present the detailed comparison of the HER performance of the present work with different catalysts and summarize the data in Table S1. Therefore, our homostructured MoS_2 catalysts show outstanding catalytic performance among the MoS_2-based HER electrocatalysts.

The cyclic stability is another important factor to evaluate the overall performance of an electrocatalyst, and therefore we investigate the cycling stability of vh-MoS_2-2 electrode by conducting the LSV scanning before and after repeated cyclic voltammetry testing in the working voltage range. As exhibited in Figure 5d, the vh-MoS_2-2 electrode exhibits an outstanding durability in a long-term process with negligible loss of current density even after 5000 cycles. The slight decay might be ascribed to the consumption of H^+ in the solution or the remaining large hydrogen bubbles on the electrode surface that hinder the reaction. The durability of vh-MoS_2-2 is also conducted using a typical I−t curve at an overpotential of ~200 mV. The I−t curve in Figure S8 indicates that even after a long period of 50 000 s the current density of the vh-MoS_2-2 electrode displays only a slight degradation. Moreover, the inserted figure exhibits the serrate shape of time dependence curve, which can be ascribed to the alternate bubble accumulation and bubble release process.[63,64]

Therefore, the significantly enhanced electrochemical HER activity can be ascribed to the following reasons, as demonstrated in Figure 5e. (1) The vh-MoS_2-2 with an edge-to-edge configuration of MoS_2 nanosheets shows more exposed edge sites (demonstrated as red arrays in Figure 5e). (2) The hierarchical vh-MoS_2-2 with well-defined interior voids leads to larger surface area, which shortens the ion diffusion distance (demonstrated as golden arrays in Figure 5e). (3) The coexistence of 2H- and 1T-phases within vh-MoS_2-2 greatly facilitates a fast electron transfer between electrode and electrolyte (demonstrated as blue arrays in Figure 5e). (4) Additional exposed active sites are successfully introduced on the basal plane of 1T-phase MoS_2 sheets (demonstrated as black spots in Figure 5e).[37]

4. CONCLUSIONS

In summary, we present a solution-processed method to prepare all-MoS_2 homostructures with vertically aligned 1T-phase syn-MoS_2 grown on the 2H-phase exf-MoS_2. The exf-MoS_2 template with a large aspect ratio contributes an ideal growing surface for the 1T-phase syn-MoS_2. Likewise, due to the presence of syn-MoS_2, the tendency of agglomeration and restacking of exf-MoS_2 nanosheets is effectively avoided. The resultant all-MoS_2 homostructures exhibit a superior HER catalytic activity with a low overpotential of 116 mV at 10 mA cm^{-2}, small Tafel slope of 60 mV dec^{-1}, and remarkable cyclic stability, due to the synergistic effect with improved exposed active sites as well as enhanced metallic conductivity in the hierarchical polymorphous MoS_2 homostructures. This simple and efficient approach might be extended to design and synthesize TMD-based homostructured materials for high-performance HER catalysis and other energy-based applications.

■ ASSOCIATED CONTENT

Ⓢ Supporting Information

The Supporting Information is available free of charge on the ACS Publications website at DOI: 10.1021/acsami.6b11298.

> Digital images showing the suspensions of exf-MoS_2 in DMF, SEM images of vh-MoS_2-2 at low magnification, SEM images of vh-MoS_2-1 and vh-MoS_2-3 at high and low magnifications, nitrogen adsorption−desorption isotherms and pore size distributions of exf-MoS_2, syn-MoS_2, and vh-MoS_2-2, Tafel plot of vh-MoS_2-2 in the region of low current densities, comparison of polarization curves between neat vh-MoS_2-2 and vh-MoS_2-2 with carbon black additives, durability of vh-MoS_2-2 at an overpotential of 200 mV, comparison of literature catalytic properties of representative noble-metal-free HER electrocatalysts (PDF)

■ AUTHOR INFORMATION

Corresponding Authors

*E-mail: czhang@dhu.edu.cn.
*E-mail: txliu@dhu.edu.cn or txliu@fudan.edu.cn.

Notes

The authors declare no competing financial interest.

■ ACKNOWLEDGMENTS

We are grateful for the financial support from the National Natural Science Foundation of China (Grants 21504012, 51125011, 51433001, and 21501091) and the Fundamental

Research Funds for the Central Universities of China (No. 16D110617).

REFERENCES

(1) Faber, M. S.; Jin, S. Earth-Abundant Inorganic Electrocatalysts and Their Nanostructures for Energy Conversion Applications. *Energy Environ. Sci.* **2014**, *7*, 3519−3542.

(2) Mallouk, T. E. Water Electrolysis: Divide and Conquer. *Nat. Chem.* **2013**, *5*, 362−363.

(3) Turner, J.; Sverdrup, G.; Mann, M. K.; Maness, P. C.; Kroposki, B.; Ghirardi, M.; Evans, R. J.; Blake, D. Renewable Hydrogen Production. *Int. J. Energy Res.* **2008**, *32*, 379−407.

(4) Walter, M. G.; Warren, E. L.; McKone, J. R.; Boettcher, S. W.; Mi, Q.; Santori, E. A.; Lewis, N. S. Solar Water Splitting Cells. *Chem. Rev.* **2010**, *110*, 6446−6473.

(5) Dunn, S. Hydrogen Futures: Toward a Sustainable Energy System. *Int. J. Hydrogen Energy* **2002**, *27*, 235−264.

(6) Cheng, L.; Huang, W.; Gong, Q.; Liu, C.; Liu, Z.; Li, Y.; Dai, H. Ultrathin WS2 Nanoflakes as a High-Performance Electrocatalyst for the Hydrogen Evolution Reaction. *Angew. Chem., Int. Ed.* **2014**, *53*, 7860−7863.

(7) Ma, Z. H.; Zhao, X. W.; Gong, C. H.; Zhang, J. W.; Zhang, J. W.; Gu, X. F.; Tong, L.; Zhou, J. F.; Zhang, Z. J. Preparation of a Graphene-Based Composite Aerogel and the Effects of Carbon Nanotubes on Preserving the Porous Structure of the Aerogel and Improving Its Capacitor Performance. *J. Mater. Chem. A* **2015**, *3*, 13445−13452.

(8) Yu, Y.; Huang, S.-Y.; Li, Y.; Steinmann, S. N.; Yang, W.; Cao, L. Layer-Dependent Electrocatalysis of MoS2 for Hydrogen Evolution. *Nano Lett.* **2014**, *14*, 553−558.

(9) Sun, X.; Zhu, X.; Zhang, N.; Guo, J.; Guo, S.; Huang, X. Controlling and Self Assembling of Monodisperse Platinum Nanocubes as Efficient Methanol Oxidation Electrocatalysts. *Chem. Commun.* **2015**, *51*, 3529−3532.

(10) Bu, L. Z.; Ding, J. B.; Guo, S. J.; Zhang, X.; Su, D.; Zhu, X.; Yao, J. L.; Guo, J.; Lu, G.; Huang, X. Q. A General Method for Multimetallic Platinum Alloy Nanowires as Highly Active and Stable Oxygen Reduction Catalysts. *Adv. Mater.* **2015**, *27*, 7204−7212.

(11) Yan, Y.; Xia, B.; Qi, X.; Wang, H.; Xu, R.; Wang, J.-Y.; Zhang, H.; Wang, X. Nano-Tungsten Carbide Decorated Graphene as Co-Catalysts for Enhanced Hydrogen Evolution on Molybdenum Disulfide. *Chem. Commun.* **2013**, *49*, 4884−4886.

(12) Chen, Z.; Cummins, D.; Reinecke, B. N.; Clark, E.; Sunkara, M. K.; Jaramillo, T. F. Core-Shell MoO3-MoS2 Nanowires for Hydrogen Evolution: A Functional Design for Electrocatalytic Materials. *Nano Lett.* **2011**, *11*, 4168−4175.

(13) Zhu, H.; Lyu, F.; Du, M.; Zhang, M.; Wang, Q.; Yao, J.; Guo, B. Design of Two-Dimensional, Ultrathin MoS2 Nanoplates Fabricated within One-Dimensional Carbon Nanofibers with Thermosensitive Morphology: High-Performance Electrocatalysts for the Hydrogen Evolution Reaction. *ACS Appl. Mater. Interfaces* **2014**, *6*, 22126−22137.

(14) Wang, D.-Y.; Gong, M.; Chou, H.-L.; Pan, C.-J.; Chen, H.-A.; Wu, Y.; Lin, M.-C.; Guan, M.; Yang, J.; Chen, C.-W.; et al. Highly Active and Stable Hybrid Catalyst of Cobalt-Doped FeS2 Nanosheets-Carbon Nanotubes for Hydrogen Evolution Reaction. *J. Am. Chem. Soc.* **2015**, *137*, 1587−1592.

(15) Tan, C.; Zhang, H. Two-Dimensional Transition Metal Dichalcogenide Nanosheet-Based Composites. *Chem. Soc. Rev.* **2015**, *44*, 2713−2731.

(16) Ding, J.; Zhou, Y.; Li, Y.; Guo, S.; Huang, X. MoS2 Nanosheet Assembling Superstructure with Three-Dimensional Ion Accessible Site: A New Class of Bifunctional Material for Battery and Electrocatalysis. *Chem. Mater.* **2016**, *28*, 2074−2080.

(17) Yin, Z. Y.; Li, H.; Li, H.; Jiang, L.; Shi, Y. M.; Sun, Y. H.; Lu, G.; Zhang, Q.; Chen, X. D.; Zhang, H. Single-Layer MoS2 Phototransistors. *ACS Nano* **2012**, *6*, 74−80.

(18) Xu, X.; Fan, Z.; Yu, X.; Ding, S.; Yu, D.; Lou, X. W. D. A Nanosheets-on-Channel Architecture Constructed from MoS2 and CMK-3 for High-Capacity and Long-Cycle-Life Lithium Storage. *Adv. Energy Mater.* **2014**, *4*, 1100902.

(19) Chang, K.; Chen, W. L-Cysteine-Assisted Synthesis of Layered MoS2/Graphene Composites with Excellent Electrochemical Performances for Lithium Ion Batteries. *ACS Nano* **2011**, *5*, 4720−4728.

(20) Cao, X.; Shi, Y.; Shi, W.; Rui, X.; Yan, Q.; Kong, J.; Zhang, H. Preparation of MoS2-Coated Three-Dimensional Graphene Networks for High-Performance Anode Material in Lithium-Ion Batteries. *Small* **2013**, *9*, 3433−3438.

(21) Wang, J. Z.; Lu, L.; Lotya, M.; Coleman, J. N.; Chou, S. L.; Liu, H. K.; Minett, A. I.; Chen, J. Development of MoS2−CNT Composite Thin Film from Layered MoS2 for Lithium Batteries. *Adv. Energy Mater.* **2013**, *3*, 798−805.

(22) Yang, Y.; Fei, H.; Ruan, G.; Xiang, C.; Tour, J. M. Edge-Oriented MoS2 Nanoporous Films as Flexible Electrodes for Hydrogen Evolution Reactions and Supercapacitor Devices. *Adv. Mater.* **2014**, *26*, 8163−8168.

(23) Zhu, J.; Sun, W.; Yang, D.; Zhang, Y.; Hoon, H. H.; Zhang, H.; Yan, Q. Multifunctional Architectures Constructing of Pani Nanoneedle Arrays on MoS2 Thin Nanosheets for High-Energy Supercapacitors. *Small* **2015**, *11*, 4123−4129.

(24) Tang, H.; Wang, J.; Yin, H.; Zhao, H.; Wang, D.; Tang, Z. Growth of Polypyrrole Ultrathin Films on MoS2Monolayers as High-Performance Supercapacitor Electrodes. *Adv. Mater.* **2015**, *27*, 1117−1123.

(25) Zhu, H.; Du, M.; Zhang, M.; Zou, M.; Yang, T.; Wang, S.; Yao, J.; Guo, B. S-Rich Single-Layered MoS2 Nanoplates Embedded in N-Doped Carbon Nanofibers: Efficient Co-Electrocatalysts for the Hydrogen Evolution Reaction. *Chem. Commun.* **2014**, *50*, 15435−15438.

(26) Li, Y.; Wang, H.; Xie, L.; Liang, Y.; Hong, G.; Dai, H. MoS2 Nanoparticles Grown on Graphene: An Advanced Catalyst for the Hydrogen Evolution Reaction. *J. Am. Chem. Soc.* **2011**, *133*, 7296−7299.

(27) Xie, J.; Zhang, H.; Li, S.; Wang, R.; Sun, X.; Zhou, M.; Zhou, J.; Lou, X. W. D.; Xie, Y. Defect-Rich MoS2 Ultrathin Nanosheets with Additional Active Edge Sites for Enhanced Electrocatalytic Hydrogen Evolution. *Adv. Mater.* **2013**, *25*, 5807−5813.

(28) Hinnemann, B.; Moses, P. G.; Bonde, J.; Jørgensen, K. P.; Nielsen, J. H.; Horch, S.; Chorkendorff, I.; Nørskov, J. K. Biomimetic Hydrogen Evolution: MoS2 Nanoparticles as Catalyst for Hydrogen Evolution. *J. Am. Chem. Soc.* **2005**, *127*, 5308−5309.

(29) Jaramillo, T. F.; Jørgensen, K. P.; Bonde, J.; Nielsen, J. H.; Horch, S.; Chorkendorff, I. Identification of Active Edge Sites for Electrochemical H2 Evolution from MoS2 Nanocatalysts. *Science* **2007**, *317*, 100−102.

(30) Greeley, J.; Jaramillo, T. F.; Bonde, J.; Chorkendorff, I.; Nørskov, J. K. Computational High-Throughput Screening of Electrocatalytic Materials for Hydrogen Evolution. *Nat. Mater.* **2006**, *5*, 909−913.

(31) Kibsgaard, J.; Chen, Z.; Reinecke, B. N.; Jaramillo, T. F. Engineering the Surface Structure of MoS2 to Preferentially Expose Active Edge Sites for Electrocatalysis. *Nat. Mater.* **2012**, *11*, 963−969.

(32) Skúlason, E.; Karlberg, G. S.; Rossmeisl, J.; Bligaard, T.; Greeley, J.; Jónsson, H.; Nørskov, J. K. Density Functional Theory Calculations for the Hydrogen Evolution Reaction in an Electrochemical Double Layer on the Pt (111) Electrode. *Phys. Chem. Chem. Phys.* **2007**, *9*, 3241−3250.

(33) Ding, Z.; Yao, B.; Feng, J.; Zhang, J. Enhanced Rate Performance and Cycling Stability of a CoCO3-Polypyrrole Composite for Lithium Ion Battery Anodes. *J. Mater. Chem. A* **2013**, *1*, 11200−11209.

(34) Coleman, J. N.; Lotya, M.; O'Neill, A.; Bergin, S. D.; King, P. J.; Khan, U.; Young, K.; Gaucher, A.; De, S.; Smith, R. J.; et al. Two-Dimensional Nanosheets Produced by Liquid Exfoliation of Layered Materials. *Science* **2011**, *331*, 568−571.

(35) Lukowski, M. A.; Daniel, A. S.; Meng, F.; Forticaux, A.; Li, L.; Jin, S. Enhanced Hydrogen Evolution Catalysis from Chemically

Exfoliated Metallic MoS2 Nanosheets. *J. Am. Chem. Soc.* **2013**, *135*, 10274−10277.

(36) Tang, H.; Dou, K.; Kaun, C.-C.; Kuang, Q.; Yang, S. MoSe2 Nanosheets and Their Graphene Hybrids: Synthesis, Characterization and Hydrogen Evolution Reaction Studies. *J. Mater. Chem. A* **2014**, *2*, 360−364.

(37) Voiry, D.; Salehi, M.; Silva, R.; Fujita, T.; Chen, M.; Asefa, T.; Shenoy, V. B.; Eda, G.; Chhowalla, M. Conducting MoS2 Nanosheets as Catalysts for Hydrogen Evolution Reaction. *Nano Lett.* **2013**, *13*, 6222−6227.

(38) Zhou, W.; Hou, D.; Sang, Y.; Yao, S.; Zhou, J.; Li, G.; Li, L.; Liuc, H.; Chen, S. MoO2 nanobelts@nitrogen self-doped MoS2 nanosheets as effective electrocatalysts for hydrogen evolution reaction. *J. Mater. Chem. A* **2014**, *2*, 11358−11364.

(39) Wang, H.; Lu, Z.; Xu, S.; Kong, D.; Cha, J. J.; Zheng, G.; Hsu, P.-C.; Yan, K.; Bradshaw, D.; Prinz, F. B. Electrochemical Tuning of Vertically Aligned MoS2 Nanofilms and Its Application in Improving Hydrogen Evolution Reaction. *Proc. Natl. Acad. Sci. U. S. A.* **2013**, *110*, 19701−19706.

(40) Yu, X. Y.; Hu, H.; Wang, Y.; Chen, H.; Lou, X. W. D. Ultrathin MoS2 Nanosheets Supported on N-Doped Carbon Nanoboxes with Enhanced Lithium Storage and Electrocatalytic Properties. *Angew. Chem., Int. Ed.* **2015**, *54*, 7395−7398.

(41) Wu, Z.; Fang, B.; Wang, Z.; Wang, C.; Liu, Z.; Liu, F.; Wang, W.; Alfantazi, A.; Wang, D.; Wilkinson, D. P. MoS2 Nanosheets: A Designed Structure with High Active Site Density for the Hydrogen Evolution Reaction. *ACS Catal.* **2013**, *3*, 2101−2107.

(42) Xie, J.; Zhang, J.; Li, S.; Grote, F.; Zhang, X.; Zhang, H.; Wang, R.; Lei, Y.; Pan, B.; Xie, Y. Controllable Disorder Engineering in Oxygen-Incorporated MoS2 Ultrathin Nanosheets for Efficient Hydrogen Evolution. *J. Am. Chem. Soc.* **2013**, *135*, 17881−17888.

(43) Wang, T.; Liu, L.; Zhu, Z.; Papakonstantinou, P.; Hu, J.; Liu, H.; Li, M. Enhanced Electrocatalytic Activity for Hydrogen Evolution Reaction from Self-Assembled Monodispersed Molybdenum Sulfide Nanoparticles on an Au Electrode. *Energy Environ. Sci.* **2013**, *6*, 625−633.

(44) Yang, L.; Zhou, W.; Lu, J.; Hou, D.; Ke, Y.; Li, G.; Tang, Z.; Kang, X.; Chen, S. Hierarchical Spheres Constructed by Defect-Rich MoS2/Carbon Nanosheets for Efficient Electrocatalytic Hydrogen Evolution. *Nano Energy* **2016**, *22*, 490−498.

(45) Zhou, W.; Zhou, K.; Hou, D.; Liu, X.; Li, G.; Sang, Y.; Liu, H.; Li, L.; Chen, S. Three-Dimensional Hierarchical Frameworks Based on MoS2 Nanosheets Self-Assembled on Graphene Oxide for Efficient Electrocatalytic Hydrogen Evolution. *ACS Appl. Mater. Interfaces* **2014**, *6*, 21534−21540.

(46) Yu, J. H.; Lee, H. R.; Hong, S. S.; Kong, D. S.; Lee, H. W.; Wang, H. T.; Xiong, F.; Wang, S.; Cui, Y. Vertical Heterostructure of Two-Dimensional MoS2 and WSe2 with Vertically Aligned Layers. *Nano Lett.* **2015**, *15*, 1031−1035.

(47) Yang, L; Zhou, W.; Hou, D.; Zhou, K.; Li, G.; Tang, Z.; Li, L.; Chen, S. Porous Metallic MoO2-Supported MoS2 Nanosheets for Enhanced Electrocatalytic Activity in the Hydrogen Evolution Reaction. *Nanoscale* **2015**, *7*, 5203−5208.

(48) O'Neill, A.; Khan, U.; Coleman, J. N. Preparation of High Concentration Dispersions of Exfoliated MoS2 with Increased Flake Size. *Chem. Mater.* **2012**, *24*, 2414−2421.

(49) Backes, C.; Berner, N. C.; Chen, X.; Lafargue, P.; LaPlace, P.; Freeley, M.; Duesberg, G. S.; Coleman, J. N.; McDonald, A. R. Functionalization of Liquid-Exfoliated Two-Dimensional 2H-MoS2. *Angew. Chem., Int. Ed.* **2015**, *54*, 2638−2642.

(50) Ge, P.; Scanlon, M. D.; Peljo, P.; Bian, X.; Vubrel, H.; O'Neill, A.; Coleman, J. N.; Cantoni, M.; Hu, X.; Kontturi, K.; et al. Hydrogen Evolution across Nano-Schottky Junctions at Carbon Supported MoS2 Catalysts in Biphasic Liquid Systems. *Chem. Commun.* **2012**, *48*, 6484−6486.

(51) Jiang, L.; Zhang, C.; Wei, J. C.; Tjiu, W. W.; Pan, J. S.; Chen, Y. W.; Liu, T. X. Surface Modifications of Halloysite Nanotubes with Superparamagnetic Fe3O4 Nanoparticles and Carbonaceous Layers for Efficient Adsorption of Dyes in Water Treatment. *Chem. Res. Chin. Univ.* **2014**, *30*, 971−977.

(52) Huang, G.; Liu, H.; Wang, S.; Yang, X.; Liu, B.; Chen, H.; Xu, M. Hierarchical Architecture of WS2 Nanosheets on Graphene Frameworks with Enhanced Electrochemical Properties for Lithium Storage and Hydrogen Evolution. *J. Mater. Chem. A* **2015**, *3*, 24128−24138.

(53) Gao, M. R.; Chan, M. K.; Sun, Y. Edge-Terminated Molybdenum Disulfide with a 9.4-Å Interlayer Spacing for Electrochemical Hydrogen Production. *Nat. Commun.* **2015**, *6*, 7493−7500.

(54) Ambrosi, A.; Sofer, Z.; Pumera, M. 2H→ 1T Phase Transition and Hydrogen Evolution Activity of MoS2, MoSe2, WS2 and WSe2 Strongly Depends on the MX2 Composition. *Chem. Commun.* **2015**, *51*, 8450−8453.

(55) Li, H.; Zhang, Q.; Yap, C. C. R.; Tay, B. K.; Edwin, T. H. T.; Olivier, A.; Baillargeat, D. From Bulk to Monolayer MoS2: Evolution of Raman Scattering. *Adv. Funct. Mater.* **2012**, *22*, 1385−1390.

(56) Wang, H.; Lu, Z.; Kong, D.; Sun, J.; Hymel, T. M.; Cui, Y. Electrochemical Tuning of MoS2 Nanoparticles on Three-Dimensional Substrate for Efficient Hydrogen Evolution. *ACS Nano* **2014**, *8*, 4940−4947.

(57) Gupta, U.; Naidu, B.; Maitra, U.; Singh, A.; Shirodkar, S. N.; Waghmare, U. V.; Rao, C. Characterization of Few-Layer 1T-MoSe2 and Its Superior Performance in the Visible-Light Induced Hydrogen Evolution Reaction. *APL Mater.* **2014**, *2*, 092802.

(58) Voiry, D.; Goswami, A.; Kappera, R.; e Silva, C. d. C. C.; Kaplan, D.; Fujita, T.; Chen, M.; Asefa, T.; Chhowalla, M. Covalent Functionalization of Monolayered Transition Metal Dichalcogenides by Phase Engineering. *Nat. Chem.* **2015**, *7*, 45−49.

(59) Calandra, M. Chemically Exfoliated Single-Layer MoS2: Stability, Lattice Dynamics, and Catalytic Adsorption from First Principles. *Phys. Rev. B: Condens. Matter Mater. Phys.* **2013**, *88*, 245428.

(60) Wang, H.; Skeldon, P.; Thompson, G. Xps Studies of MoS2 Formation from Ammonium Tetrathiomolybdate Solutions. *Surf. Coat. Technol.* **1997**, *91*, 200−207.

(61) Benson, J.; Li, M.; Wang, S.; Wang, P.; Papakonstantinou, P. Electrocatalytic Hydrogen Evolution Reaction on Edges of a Few Layer Molybdenum Disulfide Nanodots. *ACS Appl. Mater. Interfaces* **2015**, *7*, 14113−14122.

(62) Faber, M. S.; Park, K.; Cabán-Acevedo, M.; Santra, P. K.; Jin, S. Earth-Abundant Cobalt Pyrite (CoS2) Thin Film on Glass as a Robust, High-Performance Counter Electrode for Quantum Dot-Sensitized Solar Cells. *J. Phys. Chem. Lett.* **2013**, *4*, 1843−1849.

(63) Hou, Y.; Zhang, B.; Wen, Z.; Cui, S.; Guo, X.; He, Z.; Chen, J. A 3D Hybrid of Layered MoS2/Nitrogen-Doped Graphene Nanosheet Aerogels: An Effective Catalyst for Hydrogen Evolution in Microbial Electrolysis Cells. *J. Mater. Chem. A* **2014**, *2*, 13795−13800.

(64) Xie, J.; Zhang, H.; Li, S.; Wang, R.; Sun, X.; Zhou, M.; Zhou, J.; Lou, X. W.; Xie, Y. Defect-Rich MoS2 Ultrathin Nanosheets with Additional Active Edge Sites for Enhanced Electrocatalytic Hydrogen Evolution. *Adv. Mater.* **2013**, *25*, 5807−5813.

DOI: 10.1021/acsami.6b11298